ACS APPLIED MATERIALS & INTERFACES

Research Article

www.acsami.org

Decoration of Micro-/Nanoscale Noble Metal Particles on 3D Porous Nickel Using Electrodeposition Technique as Electrocatalyst for Hydrogen Evolution Reaction in Alkaline Electrolyte

Xin Qian,[†] Tao Hang,*[,†] Sangaraju Shanmugam,*[,§] and Ming Li[†]

[†]State Key Laboratory of Metal Matrix Composites, School of Material Science and Engineering, Shanghai Jiao Tong University, No. 800 Dongchuan Road, Shanghai 200240, China

[§]Department of Energy Systems Engineering, Daegu Gyeongbuk Institute of Science and Technology, 50-1 Sang-Ri, Hyeongpung-Myeon, Dalseong-gun, Daegu 711-873, South Korea

ABSTRACT: Micro-/nanoscale noble metal (Ag, Au, and Pt) particle-decorated 3D porous nickel electrodes for hydrogen evolution reaction (HER) in alkaline electrolyte are fabricated via galvanostatic electrodeposition technique. The developed electrodes are characterized by field emission scanning electron microscopy and electrochemical measurements including Tafel polarization curves, cyclic voltammetry, and electrochemical impedance spectroscopy. It is clearly shown that the enlarged real surface area caused by 3D highly porous dendritic structure has greatly reinforced the electrocatalytic activity toward HER. Comparative analysis of electrodeposited Ag, Au, and Pt particle-decorated porous nickel electrodes for HER indicates that both intrinsic property and size of the noble metal particles can lead to distinct catalytic activities. Both nanoscale Au and Pt particles have further reinforcement effect toward HER, whereas microscale Ag particles exhibit the reverse effect. As an effective 3D hydrogen evolution cathode, the nanoscale Pt-particle-decorated 3D porous nickel electrode demonstrates the highest catalytic activity with an extremely low overpotential of −0.045 V for hydrogen production, a considerable exchange current density of 9.47 mA cm^{-2} at 25 °C, and high durability in long-term electrolysis, all of which are attributed to the intrinsic catalytic property and the extremely small size of Pt particles.

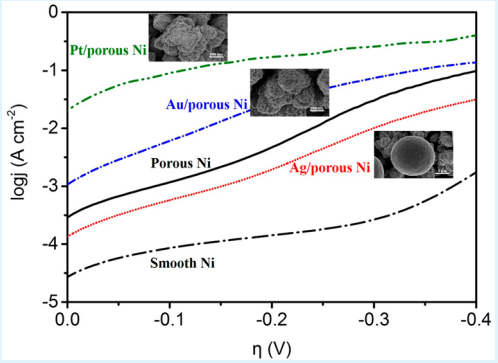

KEYWORDS: *electrodeposited noble metal particles, 3D porous nickel electrode, electrocatalyst, hydrogen evolution reaction, electrochemical impedance spectroscopy*

1. INTRODUCTION

The rapid depletion of fossil fuels and subsequent serious environmental issues have compelled researchers to search for renewable alternative energy sources.[1] Hydrogen is a clean and sustainable energy source with unlimited supply and has been considered as an effective substitute for fossil fuels. Electrochemical splitting of alkaline water has been demonstrated to be an efficient and environmentally friendly method to produce high-purity hydrogen.[2,3] However, this method requires highly efficient electrocatalyst with high current density and low overpotential for the hydrogen evolution reaction (HER).[4] Although Pt and Pt-based materials have shown exceptional performance with extremely high current density and nearly zero overpotential during HER,[5−7] the high cost and rarity of such materials inevitably impede their extensive usage and compel researchers to redirect their attention to other strategies.

One common strategy is to find earth-abundant metals or their compounds as substitutes, e.g., Ni, Co, Fe, Mo, MoS_2, and MoP.[6,8,9] Among these materials, nickel and its alloys, such as Ni−Cu, Ni−Co, Ni−Mo, Ni−Fe, Ni−Zn, and Ni−Co−Zn,[10−15] have shown high electrocatalytic performance toward HER. Furthermore, the electrocatalytic activity can be enhanced by enlarging the real surface area of the materials. A common way to enlarge the real surface area is to fabricate Raney-type alloy in order to obtain porous structures caused by the caustic leaching of active components such as Al and Zn.[16] Other methods have put great emphasis on the synthesis of catalytic electrodes with various micro-/nanostructures in order to increase the real surface area, such as macroporous Ni−Co electrode,[8] Cu−Ni foam film electrode,[15] 3D Ni nanoparticles/carbon nanotubes cathodes,[17] Ni nanowires electrode,[18] and hierarchically structured cathode.[19] Another strategy is to decrease the usage of material with high intrinsic activity (e.g., noble metal Pt) in the fabrication of electrocatalysts to minimal value so as to increase the intrinsic activity of the electrode materials with little cost.[20−27] Mahoney et al. fabricated a Pt-modified Au/C electrode with a minimal amount of platinum, and it exhibits a catalytic activity similar to that of a supported Pt/C electrode.[22] Bai et al. developed a unique synthesis

Received: January 23, 2015
Accepted: June 30, 2015
Published: June 30, 2015

DOI: 10.1021/acsami.5b00679
ACS Appl. Mater. Interfaces 2015, 7, 15716−15725

approach to prepare a Pt−Pd−rGO stack structure with controllable Pt shell thickness, and the HER performance increases dramatically as the thickness of Pt decreases substantially. Thus, it opens up new possibilities of enhancing catalytic performance with minimal usage of expensive Pt.[23]

Herein, we report a micro-/nanoscale noble metal (Ag, Au, and Pt)-particle-decorated 3D porous nickel electrode using the electrodeposition technique. In fact, this method not only eliminates the use of polymer binders but also offers a time-saving preparation for the electrode. Moreover, this idea is a proper combination of the above two strategies, namely, the main support is Ni, which exhibits the best electrocatalytic activity among non-noble materials, and its highly porous dendritic structure enlarges the real surface area of the catalyst enormously, which can enhance the electrocatalytic activity further. The electrodeposited nanoscale noble metal (Au and Pt) particles on the 3D porous nickel improve the catalytic activity and corrosion resistance dramatically. However, the electrodeposited microscale Ag particles exhibit the reverse effect and weaken the catalytic activity for HER. Figure 1 shows

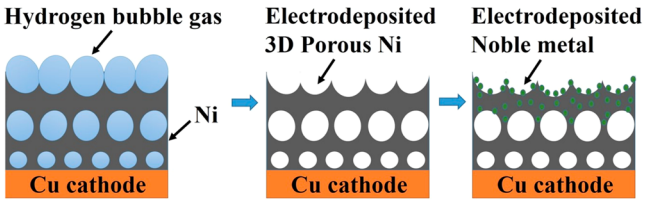

Figure 1. Schematic of fabrication procedure of micro-/nanosacle noble metal particle-decorated 3D porous nickel electrocatalyst using electrodeposition technique.

a schematic of typical fabrication procedure for a micro-/nanoscale noble metal particle-decorated 3D porous nickel electrode. This unique electrode not only provides a highly porous dendritic structure, which enlarges the real surface of the electrocatalyst enormously, but also contains size-fitted pores, which can lead to high utilization of the whole surface and facilitate the fast transport of electroactive gas bubbles through the porous electrode. Furthermore, the electrodeposited noble metal particles are distributed homogeneously on the top layer of the surface of the nickel dendrites, which enables direct and homogeneous contact with alkaline electrolyte.

2. EXPERIMENTAL SECTION

2.1. Preparation of Electrodes. The electrocatalytic materials were deposited onto the copper substrate with a working area of 2 × 2 cm^2, and the other surface areas were all covered by insulating tapes. Before electrodeposition, the copper substrate was electrolytically degreased for 30 s to remove any organic impurities. Then, it was immersed in 20 v/v % H_2SO_4 for 15 s, rinsed with deionized water, and dried by the heater blower. The electrodeposition experiments were conducted by using galvanostatic technique in different electrolytic baths. All solvents and chemicals were of reagent quality without further purification (Sinopharm Chemical Reagent). Table 1 shows the composition and concentration of chemicals used in different plating baths. The electrodeposition of smooth nickel (ED-1) was conducted under the condition of heating in a water bath at a temperature of 50 °C. The 3D porous nickel electrode (ED-2) was fabricated using hydrogen bubble template with vigorous magnetic stirring at room temperature.[28,29] The Ag plating bath was self-prepared, and the electrodeposition of Ag particles onto the as-prepared 3D porous nickel electrode (ED-3) did not require magnetic stirring. For the electrodeposition of Au and Pt because the Au plating solution was a commercialized product, the detailed composition was not provided in Table 1. The electrodeposition of Au particles onto 3D porous nickel (ED-4) requires vigorous magnetic stirring under the condition of heating in a water bath at 50 °C, whereas electrodeposition of Pt particles onto 3D porous nickel electrode (ED-5) did not require magnetic stirring. To demonstrate the reinforcement effect of 3D porous structure on the electrocatalytic activity of noble metal particles, we also electrodeposited Pt particles onto a smooth nickel electrode (ED-6) as a contrast. The electrodeposition parameters of the above six electrodes are also listed in Table 1, including current density and time.

The surface morphologies of ED-2−ED-5 were characterized with field emission scanning electron microscopy (FESEM, Siron 200), and the respective compositions were investigated by energy dispersive X-ray analyzer (EDX). Moreover, the crystal structure of electrodeposited Ag/Au/Pt catalysts was characterized by X-ray diffraction (XRD, Ultima IV), using Cu Kα (λ = 0.1541 nm) radiation in the scanning range (2θ) of 20−80° at a scanning speed of 5° min^{-1}.

2.2. Electrochemical Measurements. The electrocatalytic activities of the developed electrodes were characterized with polarization curves, cyclic voltammetry (CV), and electrochemical impedance spectroscopy (EIS). All the electrochemical tests were

Table 1. Compositions of Different Plating Baths and Operating Parameters Used in the Electrodeposition of Electrocatalytic Materials on Cu Substrate

Composition & Concentration (g L^{-1})									
smooth Ni plating bath		porous Ni plating bath		Ag plating bath		Au plating bath		Pt plating bath	
$NiSO_4·6H_2O$	250	NH_4Cl	106.7	$AgNO_3$	40	non-cyanogen		$H_2PtCl_6·6H_2O$	5.2
$NiCl_2·6H_2O$	40	$NiCl_2·6H_2O$	23.7	$Na_2S_2O_3$	225	sulfite system		H_2SO_4	49
H_3BO_3	35			$K_2S_2O_5$	40	Au: 6 ± 0.5 g L^{-1}			
$C_7H_5NO_3S$	1			$C_2H_7NO_2$	25	pH = 8−9			
$C_4H_6O_2$	0.5			CH_5N_3S	0.7				
$C_{12}H_{25}NaO_4S$	0.2								

Parameters									
	i (A cm^{-2})	t (s)	i (A cm^{-2})	t (s)	i (A cm^{-2})	t (s)	i (A cm^{-2})	t (s)	i (A cm^{-2})	t (s)
ED-1	0.03	1200								
ED-2			2.5	60						
ED-3			2.5	60	0.005	180				
ED-4			2.5	60			0.0015	60		
ED-5			2.5	60					0.025	120
ED-6	0.03	1200							0.025	120

DOI: 10.1021/acsami.5b00679
ACS Appl. Mater. Interfaces 2015, 7, 15716−15725

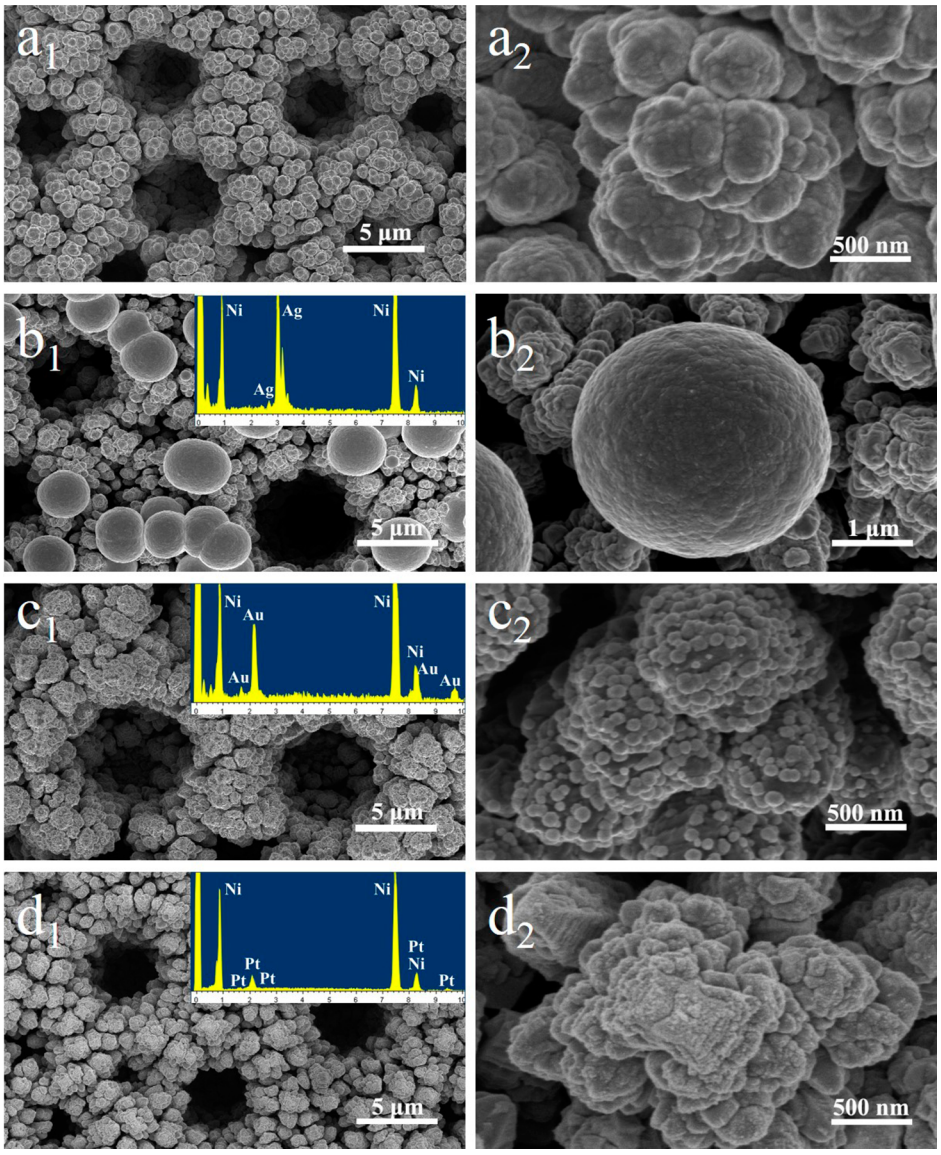

Figure 2. Top-view SEM images of ED-2 (3D porous nickel electrode), ED-3 (Ag/porous nickel electrode), ED-4 (Au/porous nickel electrode), and ED-5 (Pt/porous nickel electrode). (a_1, b_1, c_1 and d_1) Low-magnification images corresponding to ED-2, ED-3, ED-4, and ED-5, respectively (inset graphs are EDX results). (a_2, b_2, c_2 and d_2) High-magnification images corresponding to ED-2, ED-3, ED-4, and ED-5, respectively.

performed in a specially designed single-compartment cell filled with 30 wt % KOH electrolyte at room temperature (25 °C). This single-compartment cell comprised a three-electrode system in which the as-prepared electrodes acted as working electrode, a large-area platinum electrode acted as counter electrode, and a commercialized Hg|HgO|OH^- (1 M KOH electrolyte) electrode was used as reference electrode. Moreover, the distance between the surface area of working electrode and the tip of Luggin capillary equipped in the cell was less than 1 mm for the purpose of reducing variations caused by *jR* drop in the electrolyte. The holes on top of the cell allowed gas produced from HER to discharge freely. Also of note is that an electrolytic bridge was established to protect the reference electrode from being destroyed because of the great concentration gap of KOH between the HER electrolyte (30 wt %) and electrolyte stored in the reference electrode (1 M). The electrolytic bridge was a U-shaped glass tube filled with a solidified mixture of agar and KCl, one end of which was placed in the 30 wt % KOH electrolyte while the other end was placed in a beaker filled with 1 M KOH electrolyte. The reference electrode was placed in the beaker as well. All the tests were conducted in oxygen-free 30 wt % KOH solution that was degassed by bubbling Ar for 10 min before measurements.

Potentiodynamic polarization curves were recorded in the potential range from −1.5 V versus Hg|HgO|OH^- to the equilibrium potential at a scan rate of 1 mV s^{-1} for different electrodes. CV measurement was carried out on each electrode in a potential window of −1.4−0.8 V versus Hg|HgO|OH^- at a scan rate of 10 mV s^{-1}. EIS measurements were performed after obtaining the polarization curves; ac impedance spectra were recorded in the frequency range between 100 kHz and 10 mHz for ED-2−ED-4, whereas a range of 100 kHz−0.1 mHz was used for ED-5 with a 10 mV AC amplitude at different cathodic overpotentials. The complex nonlinear least-squares (CNLS) fitting of the impedance data was carried out with the Zview 3.0 software package. Furthermore, chronopotentiometry technique has been used during galvanostatic long-term electrolysis tests performed on the developed electrodes at a current density of 220 mA cm^{-2} in order to investigate the durability toward corrosion.

3. RESULTS AND DISCUSSION

Figure 2 shows the top view images of SEM investigation of ED-2−ED-5 and their EDX analyses, respectively. Figure $2a_1$ demonstrates that the pores of the porous nickel electrode are approximately 5−8 μm in diameter and are homogeneously

DOI: 10.1021/acsami.5b00679
ACS Appl. Mater. Interfaces 2015, 7, 15716−15725

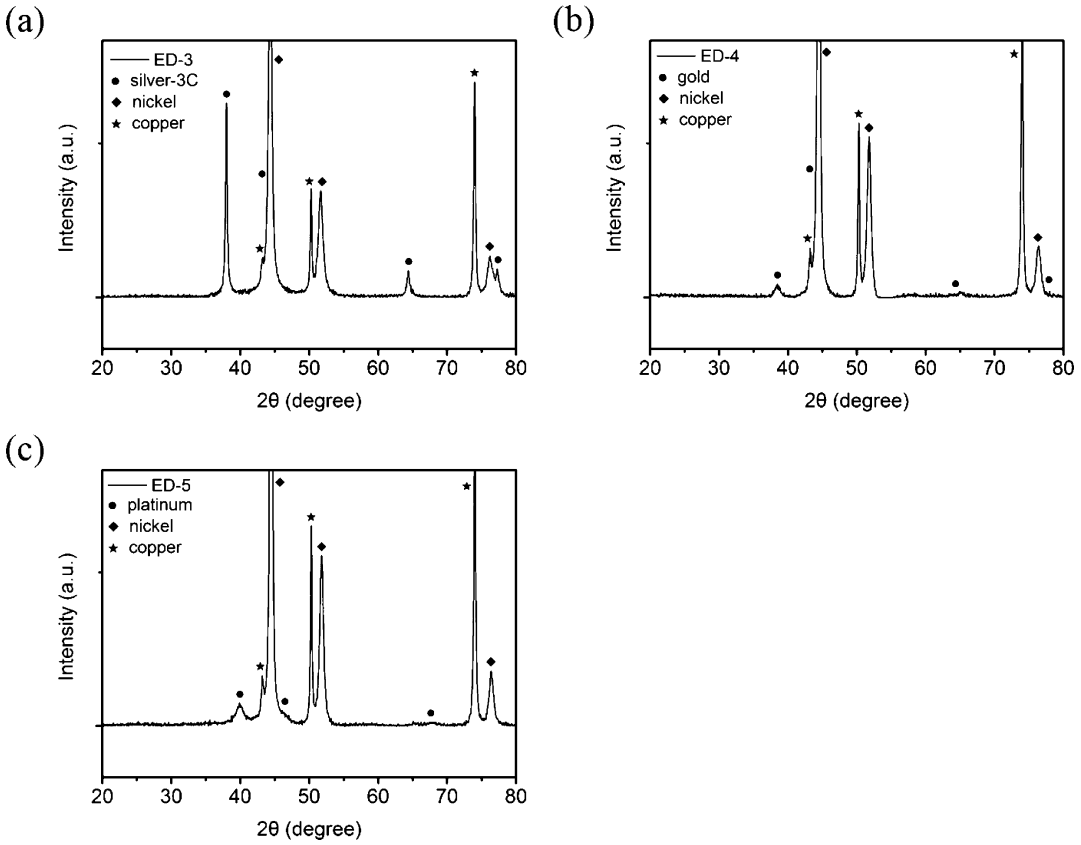

Figure 3. XRD patterns of ED-3 (Ag/porous nickel electrode), ED-4 (Au/porous nickel electrode), and ED-5 (Pt/porous nickel electrode) in the scanning range (2θ) of 20−80° at a scanning speed of 5° min^{-1}.

distributed; Figure $2a_2$ shows the magnified image of nickel dendrite, demonstrating that the 3D porous nickel electrode is composed of highly porous dendritic walls with high surface roughness. Figure $2b_1$ shows that the electrodeposited Ag particles are distributed on the surface of porous nickel electrode rather than inside the pores; these particles either grow independently or accrete together. The EDX result displayed in the inset graph shows that the mere composition of the particle is Ag. Supposing that all the applied charges are used to reduce Ag^+, the calculated maximal mass of Ag is 4.033 mg in total. Figure $2b_2$ is the magnified image of a Ag particle that is comparatively spheric with a smooth surface, and it also demonstrates that the Ag particle is approximately 2−3 μm in diameter. The fact that most of these microscale Ag particles are distributed on the tip of nickel dendrites is probably due to tip nucleation and growth. Figure $2c_1$ shows that the electrodeposited Au particles are distributed homogeneously and thickly on the top layer of the porous nickel dendrites rather than deep inside the pores, and the EDX result helps prove that the composition of the deposited particles is Au. Similarly, the calculated maximal mass of Au is 0.245 mg. Figure $2c_2$ shows the magnified image of a nickel dendrite; it clearly demonstrates that the Au particles are about 30−50 nm in diameter and are thickly distributed on the surface of nickel dendrites. Figure $2d_1$ shows the image of electrodeposited Pt-decorated porous nickel electrode. Spheric Pt particles can hardly be seen here, but the EDX result demonstrates the existence of Pt. The calculated maximal mass of Pt is 6.074 mg. Figure $2d_2$ is the magnified image of a nickel dendrite that shows the existence of extremely small Pt particles with diameter of 10−20 nm, homogeneously distributed on the top layer of the dendrite.

The XRD patterns of ED-3−ED-5 are displayed in Figure 3. In Figure 3a, apart from the diffraction peaks of substrate materials (Cu and Ni), the peaks belonging to the phase of silver-3C are observed with 2θ values of 38.06, 44.22, 64.44, and 77.46°, which correspond to the 111, 200, 220, and 311 crystal planes of silver-3C (Powder Diffraction File (PDF) no. 04-0783, International Centre for Diffraction Data (ICDD), [2004]). In Figure 3b, the peaks locate at about 38.15, 44.35, 64.53, and 77.50°, corresponding to 111, 200, 220, and 311 crystal planes of gold (PDF no. 04-0784, ICDD, [2004]), respectively. The peaks in Figure 3c that locate at about 39.74, 46.21, and 67.46° correspond to 111, 200, and 220 crystal planes (PDF no. 04-0802, ICDD, [2004]), respectively.

The electrocatalytic activity of these as-prepared electrodes are evaluated by means of potentiodynamic Tafel polarization curves in 30 wt % KOH electrolyte at 25 °C. Figure 4 shows a set of linear Tafel polarization curves on the electrodes investigated. Overpotentials are obtained as abscissa by subtracting the reversible HER equilibrium potential for each electrode. The obtained Tafel polarization curves demonstrate that ED-2 is about ten times more electroactive toward HER than ED-1, which proves that the highly porous dendritic structure with enlarged real surface area can reinforce the catalytic activity of the electrode. ED-4−ED-6 show enhanced catalytic activity, whereas ED-5 demonstrates the highest catalytic activity for HER. Because the theoretical Pt loadings of ED-5 and ED-6 are identical (maximal amount of Pt = 6.074 mg), a conclusion can also be drawn that the 3D porous structure can strongly reinforce the electrocatalytic activity of

DOI: 10.1021/acsami.5b00679
ACS Appl. Mater. Interfaces 2015, 7, 15716−15725

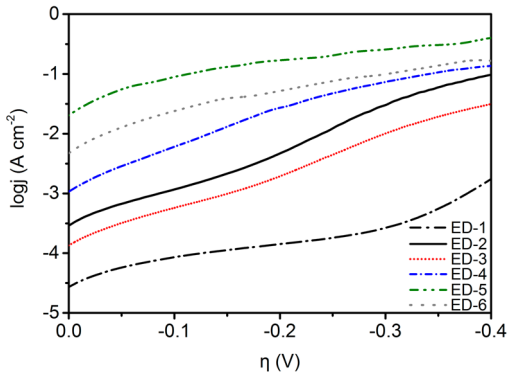

Figure 4. Linear Tafel polarization curves of these electrodes recorded in 30 wt % KOH electrolyte at 25 °C.

noble metal particles by comparing ED-5 and ED-6. However, ED-3 shows the reverse effect on the catalytic activity toward HER, that is, the catalytic activity of microscale Ag-particle-decorated porous nickel electrode is even worse than that of the porous nickel electrode; thus, it is clear that the microscale Ag particles abate the electrocatalytic activity. This reverse effect is highly attributable to the fact that the Ag particles are micrometer-sized, which can not afford adequate electroactive surface for the occurrence of HER and relatively fewer contact areas with nickel.[30,31] The Tafel polarization curves obtained in Figure 4 show a typical Tafelian behavior, indicating that the HER on these electrodes are completely controlled by the reaction kinetics expressed by the Tafel equation[32,33]

$$\eta = a + b \log j \tag{1}$$

where η (V) represents the overpotential, j (A cm^{-2}) represents the measured current density, b (V decade^{-1}) represents the cathodic Tafel slope, and a (V) is the cathodic intercept related to the exchange current density j_0 (A cm^{-2}), which is defined by the following equation:

$$a = (2.3RT)/(\beta n_e F) \times \log j_0 \tag{2}$$

where n_e represents the exchanged electrons, R (8.314 J mol^{-1} K^{-1}) is the gas constant, and F (96485 C mol^{-1}) is the Faraday constant.

Table 2 shows the cathodic Tafel slope (b) and exchange current density (j_0) obtained for all the developed electrodes. In

Table 2. Kinetic Parameters of the Hydrogen Evolution Reaction Obtained from the Tafel Polarization Curves Measured in 30 wt % KOH Alkaline Solution at 25 °C

catalytic electrode	b (mV dec^{-1})	j_0 (mA cm^{-2})
ED-1	224.22 ($\|\eta\|$<0.3) 92.94 ($\|\eta\|$>0.3)	0.02
ED-2	186.88	0.24
ED-3	170.85	0.12
ED-4	145.41	1.00
ED-5	135.59	9.47
ED-6	152.23	4.13

contrast to other electrodes, the Tafel polarization curves recorded on ED-1 show two potential-dependent regions toward HER. The Tafel slope displays a higher value at overpotentials less cathodic than −300 mV and a lower value at more cathodic overpotentials, which has already been reported in literature of smooth Ni catalysts.[33,34] The Tafel slope of ED-2 is much lower than that of ED-1, and the values of ED-3−ED-6 are also much lower than that of ED-2. As for the exchange current density, ED-1 displays the lowest value of 0.02 mA cm^{-2}, whereas for the other developed electrodes, the values are much higher. The exchange current density of ED-2 (0.24 mA cm^{-2}) is about ten times that of ED-1, which verifies the promotion effect toward HER caused by the enlarged real surface area. However, ED-3 shows a value (0.12 mA cm^{-2}) only a half of that displayed by ED-2, which is consistent with previous speculation that the electrodeposited microscale Ag particles can abate electrocatalytic activity of the electrode. In addition, ED-4 displays a value of 1.00 mA cm^{-2}, which is about 4 times that of ED-2, and ED-5 shows a value of 9.47 mA cm^{-2}, which is 40 times that of ED-2, indicating that the electrodeposited nanoscale Au and Pt particles promote the electrocatalytic activity enormously. However, despite the fact that the amount of electrodeposited Pt on ED-6 is identical to that on ED-5, ED-6 displays a current density of 4.13 mA cm^{-2}, which is only 16 times that of ED-2. It is obvious that the highly porous dendritic structure of nickel can enhance the catalytic activity dramatically. Therefore, it is clear that ED-5 possesses the best performance among all the developed electrodes.

CV measurements are also carried out on these electrodes for the purpose of obtaining the hydrogen desorption peaks and the hydrogen decomposition potentials; thus, the overpotential needed to produce hydrogen can be easily calculated. Figure 5 displays the CV results of all the developed electrodes; the hydrogen desorption peaks for different electrodes can be easily obtained. Figure 5 shows that the desorption peak at about 0.35 V exists in almost all the electrodes except ED-3, which has its own unique desorption peaks at about 0.25, 0.42, and 0.59 V. The other desorption peak at about −0.16 V is apparently seen in all the electrodes except ED-1 and ED-6; it is highly possible that this peak is either extremely weak in ED-1/ED-6 so that it can hardly be seen or that it is an exclusive phenomenon of 3D porous nickel structure. Furthermore, the hydrogen decomposition potentials of ED-1−ED-6 are −1.32, −1.20, −1.22, −1.18, −1.08, and −1.10 V, respectively.

According to the Tafel polarization curves recorded on these electrodes, the reversible HER equilibrium potential can be easily obtained and the overpotentials are used as abscissa in order to make a comparison between the current density (j) and overpotential (V) cathodic polarization curves which characterize the decomposition of hydrogen of different electrodes. Figure 6 shows the level of difficulty to produce hydrogen through comparison of hydrogen decomposition overpotentials relating to different electrodes. It is obvious that ED-5 needs the lowest overpotential for hydrogen production among all the developed electrodes. ED-4 exhibits improved catalytic activity compared with ED-2 because it requires less overpotential for hydrogen decomposition, whereas ED-3 shows diminished catalytic activity compared to ED-2 because of the additional overpotential needed to produce hydrogen.

Furthermore, the accurate overpotentials needed for hydrogen production by all the developed electrodes are listed in Table 3. The overpotential needed for ED-2 (−0.239 V) is less than half of that needed by ED-1 (−0.528 V); this data further demonstrate that the enlarged surface area caused by highly porous structure has great promotion effect toward HER. However, the overpotential needed for ED-3 (−0.333 V) is much more than that of ED-2, which certifies that the microscale Ag particles can abate the electrocatalytic activity for HER. In addition, both ED-4 (−0.173 V) and ED-5 (−0.045 V) show enhanced catalytic activity, whereas ED-5

DOI: 10.1021/acsami.5b00679
ACS Appl. Mater. Interfaces 2015, 7, 15716−15725

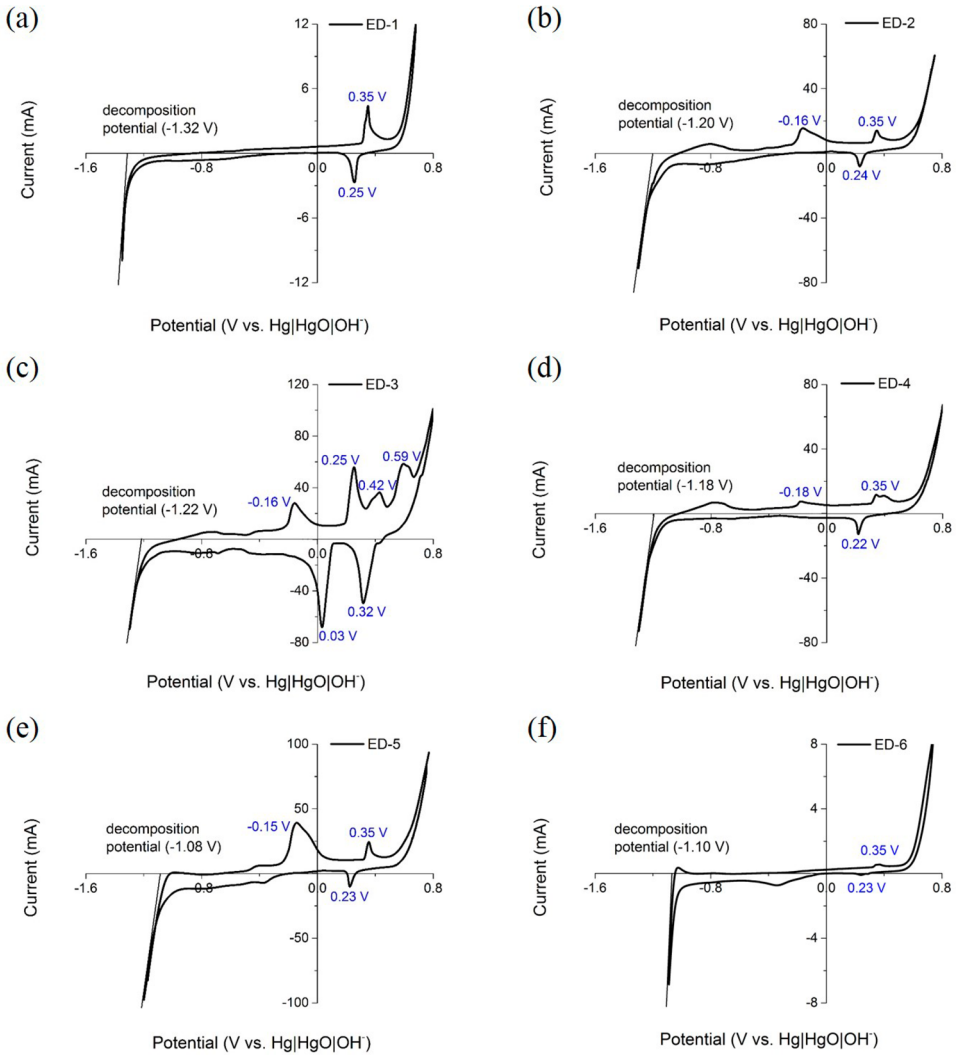

Figure 5. Cyclic voltammetry recorded on the developed electrodes in 30 wt % KOH electrolyte at 25 °C: (a) ED-1, (b) ED-2, (c) ED-3, (d) ED-4, (e) ED-5, and (f) ED-6.

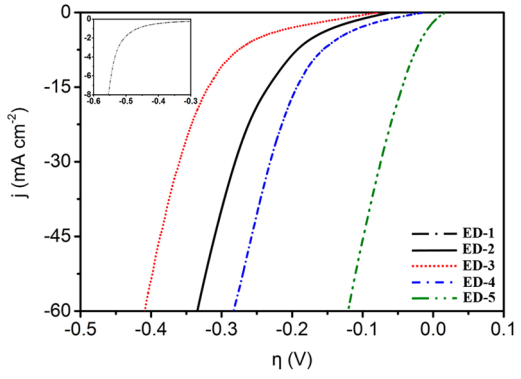

Figure 6. Cathodic polarization curves characterizing the decomposition of hydrogen of ED-2, ED-3, ED-4, and ED-5; the inset graph corresponds to the cathodic polarization curve of ED-1 (smooth nickel electrode).

displays the lowest overpotential needed to produce hydrogen among all the electrodes.

EIS measurements are also carried out on these developed electrodes at different overpotentials on the basis of the previously obtained Tafel polarization curves in 30 wt % KOH electrolyte at the temperature of 25 °C. Figure 7 shows both the Nyquist and Bode representations of ED-2−ED-5 at their selected overpotentials. It is clearly shown that two semicircles (i.e., two different time constants) are differentiated in the Nyquist representation of the impedance data recorded on ED-2 (Figure 7a_1), and two maximums exist in the Bode representation of the phase angle as a function of frequency (Figure 7a_2). The semicircles at high frequencies (HF) are independent of overpotentials, indicating a cylindrical pore geometry of the electrode, as is observed from the SEM investigations, with no mass transfer effect,[8] which indicates that the potential-independent semicircle is related to porosity

Table 3. Overpotential Needed to Reach the Hydrogen Decomposition Potential in 30 wt % KOH Alkaline Solution Regarding Different Catalytic Electrodes at 25 °C

catalytic electrode	equilibrium potential (V)	H_2 decomposition potential (V)	overpotential needed to produce H_2 (V)
ED-1	−0.792	−1.32	−0.528
ED-2	−0.961	−1.20	−0.239
ED-3	−0.887	−1.22	−0.333
ED-4	−1.007	−1.18	−0.173
ED-5	−1.035	−1.08	−0.045

DOI: 10.1021/acsami.5b00679
ACS Appl. Mater. Interfaces 2015, 7, 15716−15725

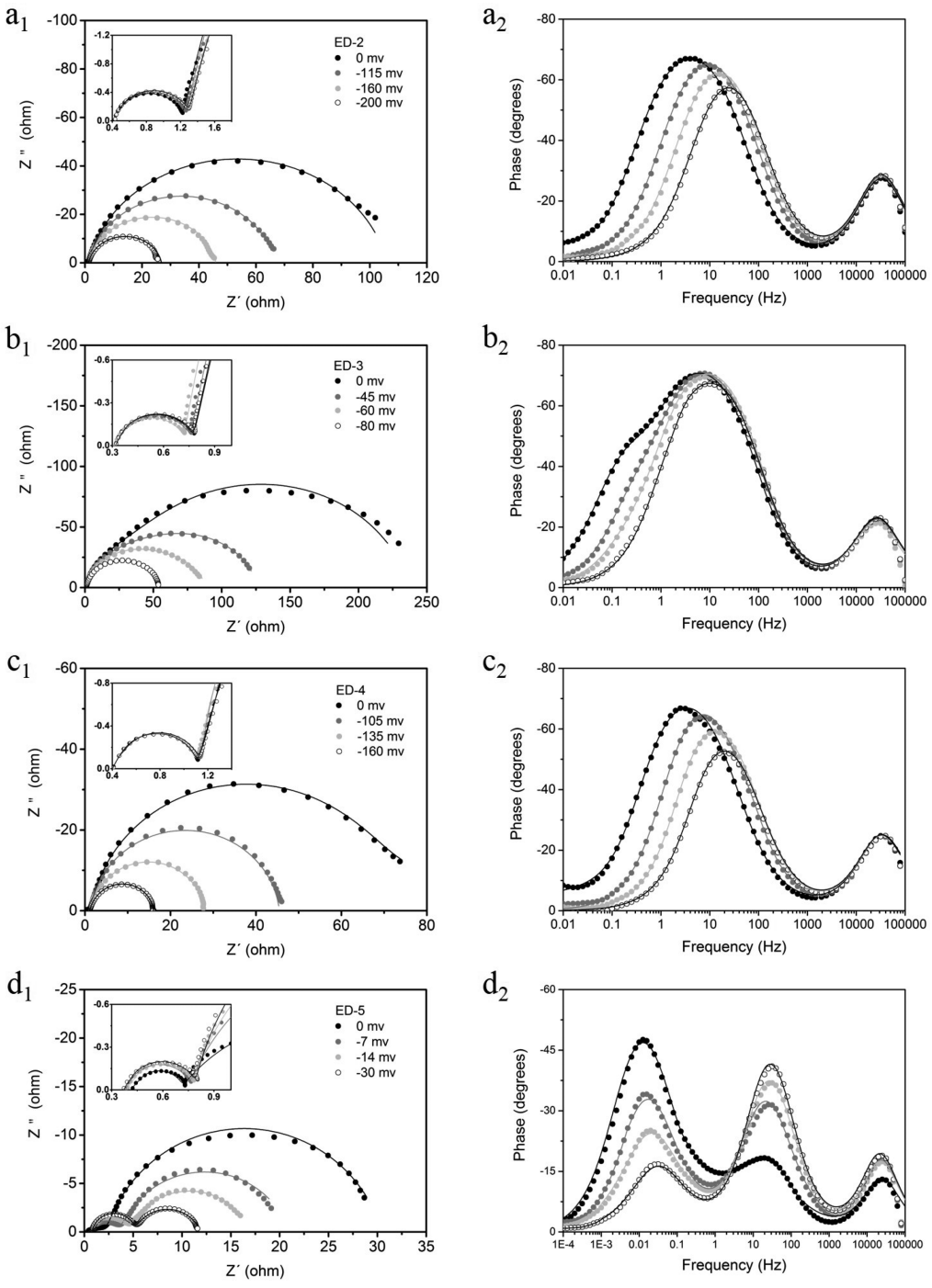

Figure 7. Impedance data at various overpotentials obtained in 30 wt % KOH electrolyte at 25 °C for the developed electrodes of ED-2, ED-3, ED-4, and ED-5, respectively: (a_1, b_1, c_1, and d_1) Nyquist representations. (a_2, b_2, c_2, and d_2) Bode representations. Symbols are the experimental points, and solid lines are modeled data.

of the electrode surface. However, the diameter of the other semicircle at low frequencies (LF) decreases as the overpotential gets more cathodic, indicating that the potential-dependent semicircle is associated with HER kinetics.[35] With respect to ED-3 and ED-4, the Nyquist representations of the impedance data (Figure $7b_1$,c_1) reveal that one semicircle is clearly differentiated and the other two semicircles are strongly overlapped (i.e., three different time constants), and the Bode representations also show two maximums (Figure $7b_2$ and Figure $7c_2$). In contrast, the Nyquist representation of impedance data recorded on ED-5 (Figure $7d_1$) demonstrates that three semicircles are clearly differentiated (i.e., three time constants), which is also verified by the presence of three maximums in the Bode representation (Figure $7d_2$). The small semicircle at HF is similar to that of ED-2; thus, the potential-independent semicircle is related to surface porosity. However, it is shown that as the cathodic overpotential increases the diameter of the other two semicircles at relatively LF (strongly overlapped for ED-3 and ED-4, but clearly differentiated for ED-5) apparently decreases, indicating that at least one of the two potential-dependent semicircles is associated with HER kinetics.

DOI: 10.1021/acsami.5b00679
ACS Appl. Mater. Interfaces 2015, 7, 15716−15725

To model the experimental data of the impedance response characterized by two semicircles in the Nyquist representation of ED-2, a two-time-constant parallel (2TP) electric equivalent circuit (EEC) model (Figure 8a) proposed by Armstrong and

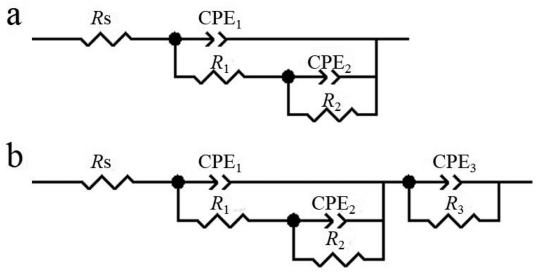

Figure 8. EEC models used to explain the EIS responses of the HER on developed electrodes: (a) two-time constant parallel model (2TP), (b) three-time constant model (3T).

Henderson[36] is applied to fit the EIS response. For this EEC model, the double-layer capacitance is replaced by a CPE (constant phase element),[35] defined in impedance representation as shown in eq 3

$$Z_{\mathrm{CPE}} = [\mathrm{CPE(T)}(i\omega)^{\mathrm{CPE(P)}}]^{-1} \quad (3)$$

where CPE(T) is the CPE constant, ω is the angular frequency (rad s^{-1}), $i^2 = -1$ is the imaginary number, and CPE(P) is the CPE exponent. In addition, the HF time constant, τ_1 (CPE_1, R_1), is related to HER charge-transfer kinetics, whereas the LF time constant, τ_2 (CPE_2, R_2), is associated with hydrogen adsorption.[12,32,35]

With respect to the impedance characterized by three semicircles in the Nyquist representation, in order to obtain a clear picture of the HER occurring at the electrode/electrolyte interface, a three-time-constant (3T) EEC model (see Figure 8b) is proposed to fit the EIS response. For this model, the first HF time constant, τ_1 (CPE_1, R_1), is related to HER charge-transfer kinetics, the second time constant τ_2 (CPE_2, R_2), and the third time constant τ_3 (CPE_3, R_3) is associated with hydrogen adsorption and HER charge-transfer kinetics.

Figure 7 shows that a good agreement between the experimental points (symbols) and CNLS approximations (solid lines) is obtained when the 2TP model is used to fit impedance data of ED-2 and when the 3T model is used to fit data of ED-3–ED-5. Table 4 shows the best-fit estimates of EEC parameters obtained by fitting the EIS experimental data of ED-2 and ED-5 at different selected overpotentials. The average double-layer capacitance, C_i, for the porous structure is calculated using eq 4 proposed by Brug et al.[37]

$$C_i = \left[\frac{\mathrm{CPE(T)}_i}{(R_S^{-1} + R_i^{-1})^{(1-\mathrm{CPE(P)}_i)}}\right]^{1/\mathrm{CPE(P)}_i} \quad (4)$$

Table 4. EEC Parameters Obtained by Fitting EIS Experimental Data Collected at Different Overpotentials in 30 wt % KOH Alkaline Solution on Different Catalytic Electrodes at 25 °C

		ED-2		
η (mV)	0	−115	−160	−200
R_S (Ω cm^2)	0.51	0.51	0.52	0.52
R_1 (Ω cm^2)	0.87	0.92	0.96	0.96
R_2 (Ω cm^2)	118.41	73.94	50.45	28.86
$CPE(T)_1$	1.04×10^{-5}	9.98×10^{-5}	9.56×10^{-5}	
$CPE(P)_1$	1.00	1.00	1.00	1.00
C_1 (mF cm^{-2})	9.22×10^{-3}	8.83×10^{-3}	8.46×10^{-3}	8.56×10^{-3}
$CPE(T)_2$	5.10×10^{-3}	2.86×10^{-3}	2.19×10^{-3}	1.91×10^{-3}
$CPE(P)_2$	0.87	0.89	0.90	0.90
C_2 (mF cm^{-2})	1.91	1.14	0.86	0.78
τ_1 (s)	8.05×10^{-6}	8.13×10^{-6}	8.11×10^{-6}	8.23×10^{-6}
τ_2 (s)	48.88×10^{-2}	15.31×10^{-2}	7.43×10^{-2}	3.49×10^{-2}
		ED-5		
η (mV)	0	−7	−14	−30
R_S (Ω cm^2)	0.50	0.45	0.47	0.45
R_1 (Ω cm^2)	0.30	0.40	0.41	0.45
R_2 (Ω cm^2)	1.80	3.25	4.16	4.93
R_3 (Ω cm^2)	31.85	19.67	14.31	7.66
$CPE(T)_1$	3.05×10^{-5}	2.73×10^{-5}	2.62×10^{-5}	2.61×10^{-5}
$CPE(P)_1$	1.00	1.00	1.00	1.00
C_1 (mF cm^{-2})	2.69×10^{-2}	2.41×10^{-2}	2.31×10^{-2}	2.31×10^{-2}
$CPE(T)_2$	69.05×10^{-3}	12.84×10^{-3}	7.61×10^{-3}	5.39×10^{-3}
$CPE(P)_2$	0.67	0.83	0.87	0.91
C_2 (mF cm^{-2})	9.71	3.76	2.76	2.48
$CPE(T)_3$	1.07	0.80	0.70	
$CPE(P)_3$	0.83	0.79	0.75	
C_3 (mF cm^{-2})	808.8	520.6	399.9	
τ_1 (s)	8.10×10^{-6}	9.25×10^{-6}	9.41×10^{-6}	10.38×10^{-6}
τ_2 (s)	3.70×10^{-2}	1.88×10^{-2}	1.62×10^{-2}	1.58×10^{-2}
τ_3 (s)	61.44	28.28	18.24	8.69

DOI: 10.1021/acsami.5b00679
ACS Appl. Mater. Interfaces 2015, 7, 15716–15725

According to the EEC parameters listed in Table 4 for ED-2 (2TP model), both the CPE_1 and C_1 decrease as R_1 increases with an increase in the cathodic overpotential and the τ_1 almost doesn't change, which is consistent with the typical behavior related to the response of pores.[35,38] Hence, the first time constant, τ_1 (CPE_1, R_1) or HF constant, is related to the surface porosity of the electrode, that is, to the surface porosity pseudocapacitance characterized by CPE_1 and resistance characterized by R_1. In contrast, the second time constant exhibits a different behavior: τ_2 decreases with the cathodic overpotential, indicating that this semicircle is related to the kinetics of the process. CPE_2, R_2, and C_2 decrease as the cathodic overpotential increases. Therefore, it can be concluded that the second time constant, τ_2 (CPE_2, R_2) or LF time constant, is associated with HER charge-transfer kinetics, namely, with the response of double-layer capacitance, characterized by CPE_2, and HER charge-transfer resistance, characterized by R_2.

With respect to ED-5 (3T model), from Table 4 it is clear that τ_1 almost doesn't change, both the CPE_1 and C_1 decrease, and R_1 increases as the overpotential become more cathodic, which indicates that the first time constant, τ_1 (CPE_1, R_1), is related to the surface porosity of the electrode. In contrast, both τ_2 and τ_3 decrease with the overpotential, indicating that both time constants are related to kinetics of the process; this is highly attributable to the simultaneous HER happening on different metal/electrolyte interfaces created by the coexposure of Ni and Pt to the alkaline electrolyte. However, the difference is that τ_2 displays a very slight decrease compared with the dramatic decrease of τ_3; it is obvious that the difference in physical property and catalytic activity of Ni and Pt causes this phenomenon. Both CPE_2 and C_2 decrease slightly; thus, the second time constant, τ_2 (CPE_2, R_2), is supposed to be related to the HER charge-transfer kinetics of nickel. In addition, τ_3, CPE_3, C_3 and R_3 decreases obviously with the cathodic overpotential, thus the third time constant, τ_3 (CPE_3, R_3) is associated with HER charge-transfer kinetics of Pt nanoparticles. Despite the best-fit estimates of EEC parameters of ED-3 and ED-4 (not presented here), they exhibit behavior similar to that of ED-5, indicating that the first time constant is related to the surface porosity of the electrode, whereas the second and the third time constants are associated with HER charge-transfer kinetics of nickel and noble metal particles, respectively.

Because corrosion has been regarded as a tricky problem for electrocatalysts, a series of galvanostatic long-term electrolysis tests were performed on the developed electrodes at a current density of 220 mA cm^{-2} to investigate anticorrosion performance. The above analysis has demonstrated that ED-5 exhibits the best electrocatalytic activity toward HER compared to other electrodes and that it possesses the greatest potential to be applied to industrial production of hydrogen from alkaline water, so the galvanostatic long-term electrolysis test focuses on ED-5. Chronopotentiometry technique has been used during the long-term electrolysis test, and the result is shown in Figure 9. The potential recorded for ED-5 decreases sharply in the first hour, and then it reaches a steady value of about −1.47 V versus Hg|HgO|OH^- with very small potential oscillations in the following time. Therefore, the Pt-nanoparticle-decorated porous nickel electrode can be considered rather stable during long-time electrolysis and a very promising electrocatalyst for industrial production of hydrogen from alkaline electrolyte.

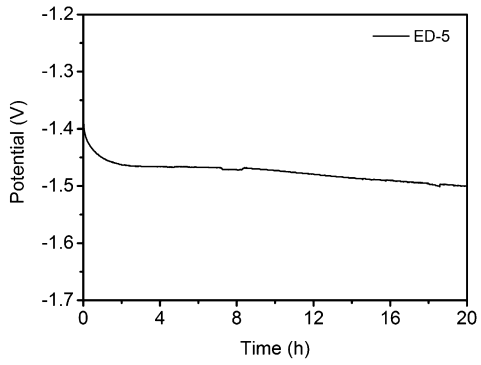

Figure 9. Galvanostatic long-term electrolysis test performed on ED-5 at a current density of 220 mA cm^{-2} in 30 wt % KOH alkaline electrolyte at 25 °C.

4. CONCLUSIONS

Decoration of micro-/nanoscale noble metal particles on 3D porous nickel as catalytic electrodes for HER in 30 wt % KOH electrolyte are successfully fabricated using electrodeposition technique. It is clearly shown that the enlarged real surface area caused by 3D highly porous dendritic structure has a great reinforcement effect in electrocatalytic activity toward HER. Among the specially designed electrodes, both nanoscale Au and Pt particles enhance catalytic activity for HER dramatically, despite Pt particles exhibiting much more superior performance than Au particles. On the contrary, the microscale Ag particles abate the catalytic activity toward HER; this reverse effect is highly attributable to the fact that the Ag particles are micrometer-sized, which can not afford adequate electroactive surface for occurrence of HER and relatively fewer contact areas with nickel. Moreover, the electrocatalytic performance of these fabricated electrodes are verified by Tafel polarization curves, CV results, and ac impedance data. The results of these electrochemical measurements show good consistency in the determination of the best electrode. The nanoscale Pt-particle-decorated 3D porous nickel electrode exhibits the largest exchange current density (9.47 mA cm^{-2}), the lowest overpotential needed for hydrogen production (−0.045 V), and the least impedance and little consumption of Pt as well as high durability after long-term electrolysis. Hence, this unique electrode has great potential to be used in hydrogen production industry with low cost, high efficiency, and long durability.

AUTHOR INFORMATION

Corresponding Authors

*E-mail: hangtao@sjtu.edu.cn. Fax: +86-21-3420-2748. Tel: +86-21-3420-2748.

*E-mail: sangarajus@dgist.ac.kr.

Notes

The authors declare no competing financial interest.

ACKNOWLEDGMENTS

This work is sponsored by National Natural Science Foundation of China (no. 21303100) and Shanghai Natural Science Foundation (no. 13ZR1420400).

REFERENCES

(1) Chow, J.; Kopp, R. J.; Portney, P. R. Energy Resources and Global Development. *Science* **2003**, *302*, 1528−1531.

(2) Turner, J. A. Sustainable Hydrogen Production. *Science* **2004**, *305*, 972−974.

DOI: 10.1021/acsami.5b00679
ACS Appl. Mater. Interfaces 2015, 7, 15716−15725

(3) Gray, H. B. Powering the Planet with Solar Fuel. *Nat. Chem.* **2009**, *1*, 7−7.
(4) Walter, M. G.; Warren, E. L.; McKone, J. R.; Boettcher, S. W.; Mi, Q.; Santori, E. A.; Lewis, N. S. Solar Water Splitting Cells. *Chem. Rev.* **2010**, *110*, 6446−6473.
(5) Volbeda, A.; Fontecilla-Camps, J. C. The Active Site and Catalytic Mechanism of NiFe Hydrogenases. *Dalton Trans.* **2003**, 4030−4038.
(6) Shima, S.; Pilak, O.; Vogt, S.; Schick, M.; Stagni, M. S.; Meyer-Klaucke, W.; Warkentin, E.; Thauer, R. K.; Ermler, U. The Crystal Structure of [Fe]-Hydrogenase Reveals the Geometry of the Active Site. *Science* **2008**, *321*, 572−575.
(7) Sheng, W.; Gasteiger, H. A.; Shao-Horn, Y. Hydrogen Oxidation and Evolution Reaction Kinetics on Platinum: Acid vs Alkaline Electrolytes. *J. Electrochem. Soc.* **2010**, *157*, B1529−B1536.
(8) González-Buch, C.; Herraiz-Cardona, I.; Ortega, E.; García-Antón, J.; Pérez-Herranz, V. Synthesis and Characterization of Macroporous Ni, Co and Ni−Co Electrocatalytic Deposits for Hydrogen Evolution Reaction in Alkaline Media. *Int. J. Hydrogen Energy* **2013**, *38*, 10157−10169.
(9) Xiao, P.; Sk, M. A.; Thia, L.; Ge, X. M.; Lim, R. J.; Wang, J. Y.; Lim, K. H.; Wang, X. Molybdenum Phosphide as an Efficient Electrocatalyst for the Hydrogen Evolution Reaction. *Energy Environ. Sci.* **2014**, *7*, 2624−2629.
(10) Solmaz, R.; Kardaş, G. Electrochemical Deposition and Characterization of NiFe Coatings as Electrocatalytic Materials for Alkaline Water Electrolysis. *Electrochim. Acta* **2009**, *54*, 3726−3734.
(11) Solmaz, R.; Döner, A.; Şahin, İ.; Yüce, A.; Kardaş, G.; Yazıcı, B.; Erbil, M. The Stability of NiCoZn Electrocatalyst for Hydrogen Evolution Activity in Alkaline Solution During Long-Term Electrolysis. *Int. J. Hydrogen Energy* **2009**, *34*, 7910−7918.
(12) Herraiz-Cardona, I.; Ortega, E.; Perez-Herranz, V. Impedance Study of Sydrogen Evolution on Ni/Zn and Ni-Co/Zn Stainless Steel Based Electrodeposits. *Electrochim. Acta* **2011**, *56*, 1308−1315.
(13) Tasic, G. S.; Maslovara, S. P.; Zugic, D. L.; Maksic, A. D.; Marceta Kaninski, M. P. Characterization of the Ni−Mo Catalyst Formed in situ During Hydrogen Generation from Alkaline Water Electrolysis. *Int. J. Hydrogen Energy* **2011**, *36*, 11588−11595.
(14) Herraiz-Cardona, I.; Ortega, E.; Vázquez-Gómez, L.; Pérez-Herranz, V. Double-Template Fabrication of Three-Dimensional Porous Nickel Electrodes for Hydrogen Evolution Reaction. *Int. J. Hydrogen Energy* **2012**, *37*, 2147−2156.
(15) Zhang, J.; Baro, M. D.; Pellicer, E.; Sort, J. Electrodeposition of Magnetic, Superhydrophobic, Non-Stick, Two-Phase Cu-Ni Foam Films and Their Enhanced Performance for Hydrogen Evolution Reaction in Alkaline Water Media. *Nanoscale* **2014**, *6*, 12490−12499.
(16) Anantharaman, V.; Pintauro, P. The Electrocatalytic Hydrogenation of Glucose I. Kinetics of Hydrogen Evolution and Glucose Hydrogenation on Raney Nickel Powder. *J. Electrochem. Soc.* **1994**, *141*, 2729−2741.
(17) McArthur, M. A.; Jorge, L.; Coulombe, S.; Omanovic, S. Synthesis and Characterization of 3D Ni Nanoparticle/Carbon Nanotube Cathodes for Hydrogen Evolution in Alkaline Electrolyte. *J. Power Sources* **2014**, *266*, 365−373.
(18) Chen, P. C.; Chang, Y. M.; Wu, P. W.; Chiu, Y. F. Fabrication of Ni Nanowires for Hydrogen Evolution Reaction in a Neutral Electrolyte. *Int. J. Hydrogen Energy* **2009**, *34*, 6596−6602.
(19) Yin, Z.; Chen, F. A Facile Electrochemical Fabrication of Hierarchically Structured Nickel−Copper Composite Electrodes on Nickel Foam for Hydrogen Evolution Reaction. *J. Power Sources* **2014**, *265*, 273−281.
(20) Dasgupta, N. P.; Liu, C.; Andrews, S.; Prinz, F. B.; Yang, P. Atomic Layer Deposition of Platinum Catalysts on Nanowire Surfaces for Photoelectrochemical Water Reduction. *J. Am. Chem. Soc.* **2013**, *135*, 12932−12935.
(21) Doner, A.; Taskesen, E.; Kardas, G. Hydrogen Evolution Stability of Platinum Modified Graphite Electrode. *Int. J. Hydrogen Energy* **2014**, *39*, 11355−11359.
(22) Mahoney, E. G.; Sheng, W. C.; Yan, Y. S.; Chen, J. G. G. Platinum-Modified Gold Electrocatalysts for the Hydrogen Oxidation Reaction in Alkaline Electrolytes. *ChemElectroChem* **2014**, *1*, 2058−2063.
(23) Bai, S.; Wang, C.; Deng, M.; Gong, M.; Bai, Y.; Jiang, J.; Xiong, Y. Surface Polarization Matters: Enhancing the Hydrogen-Evolution Reaction by Shrinking Pt Shells in Pt−Pd−Graphene Stack Structures. *Angew. Chem., Int. Ed.* **2014**, *53*, 12120−12124.
(24) Cao, X.; Han, Y.; Gao, C. Z.; Xu, Y.; Huang, X. M.; Willander, M.; Wang, N. Highly Catalytic Active PtNiCu Nanochains for Hydrogen Evolution Reaction. *Nano Energy* **2014**, *9*, 301−308.
(25) van Drunen, J.; Pilapil, B. K.; Makonnen, Y.; Beauchemin, D.; Gates, B. D.; Jerkiewicz, G. Electrochemically Active Nickel Foams as Support Materials for Nanoscopic Platinum Electrocatalysts. *ACS Appl. Mater. Interfaces* **2014**, *6*, 12046−12061.
(26) Hsu, I. J.; Chen, J. G.; Jiang, X.; Willis, B. G. Atomic Layer Deposition Synthesis and Evaluation of Core-Shell Pt-WC Electrocatalysts. *J. Vac. Sci. Technol., A* **2015**, *33*, 01A129−101A129.
(27) Henning, S.; Herranz, J.; Gasteiger, H. A. Bulk-Palladium and Palladium-on-Gold Electrocatalysts for the Oxidation of Hydrogen in Alkaline Electrolyte. *J. Electrochem. Soc.* **2014**, *162*, F178−F189.
(28) Qian, X.; Hang, T.; Nara, H.; Yokoshima, T.; Li, M.; Osaka, T. Electrodeposited Three-Dimensional Porous Si−O−C/Ni Thick Film as High Performance Anode for Lithium-ion Batteries. *J. Power Sources* **2014**, *272*, 794−799.
(29) Zhang, Y. Q.; Xia, X. H.; Wang, X. L.; Mai, Y. J.; Shi, S. J.; Tang, Y. Y.; Cu, C. G.; Tu, J. P. Three-Dimensional Porous Nano-Ni Supported Silicon Composite Film for High-Performance Lithium-ion Batteries. *J. Power Sources* **2012**, *213*, 106−111.
(30) Tang, M. H.; Hahn, C.; Klobuchar, A. J.; Ng, J. W. D.; Wellendorff, J.; Bligaard, T.; Jaramillo, T. F. Nickel-Silver Alloy Electrocatalysts for Hydrogen Evolution and Oxidation in An Alkaline Electrolyte. *Phys. Chem. Chem. Phys.* **2014**, *16*, 19250−19257.
(31) Amin, M. A.; Fadlallah, S. A.; Alosaimi, G. S. In Situ Aqueous Synthesis of Silver Nanoparticles Supported on Titanium as Active Electrocatalyst for the Hydrogen Evolution Reaction. *Int. J. Hydrogen Energy* **2014**, *39*, 19519−19540.
(32) Herraiz-Cardona, I.; Ortega, E.; Antón, J. G.; Pérez-Herranz, V. Assessment of the Roughness Factor Effect and the Intrinsic Catalytic Activity for Hydrogen Evolution Reaction on Ni-Based Electrodeposits. *Int. J. Hydrogen Energy* **2011**, *36*, 9428−9438.
(33) Domínguez-Crespo, M. A.; Torres-Huerta, A. M.; Brachetti-Sibaja, B.; Flores-Vela, A. Electrochemical Performance of Ni−RE (RE = rare earth) as Electrode Material for Hydrogen Evolution Reaction in Alkaline Medium. *Int. J. Hydrogen Energy* **2011**, *36*, 135−151.
(34) Metikoš-Huković, M.; Grubač, Z.; Radić, N.; Tonejc, A. Sputter Deposited Nanocrystalline Ni and Ni-W Films as Catalysts for Hydrogen Evolution. *J. Mol. Catal. A: Chem.* **2006**, *249*, 172−180.
(35) Birry, L.; Lasia, A. Studies of the Hydrogen Evolution Reaction on Raney Nickel-Molybdenum Electrodes. *J. Appl. Electrochem.* **2004**, *34*, 735−749.
(36) Armstrong, R.; Henderson, M. Impedance Plane Display of a Reaction with an Adsorbed Intermediate. *J. Electroanal. Chem. Interfacial Electrochem.* **1972**, *39*, 81−90.
(37) Brug, G. J.; van den Eeden, A. L. G.; Sluyters-Rehbach, M.; Sluyters, J. H. The Analysis of Electrode Impedances Complicated by the Presence of a Constant Phase Element. *J. Electroanal. Chem. Interfacial Electrochem.* **1984**, *176*, 275−295.
(38) Losiewicz, B.; Budniok, A.; Rówiński, E.; Łągiewka, E.; Lasia, A. The Structure, Morphology and Electrochemical Impedance Study of the Hydrogen Evolution Reaction on the Modified Nickel Electrodes. *Int. J. Hydrogen Energy* **2004**, *29*, 145−157.

DOI: 10.1021/acsami.5b00679
ACS Appl. Mater. Interfaces 2015, 7, 15716−15725